Flow speed within the Antarctic ice sheet and its controls inferred from satellite observations

Robert J. Arthern[1], Richard C. A. Hindmarsh[1], and C. Rosie Williams[1]

[1]British Antarctic Survey, Natural Environment Research Council, Cambridge, UK

Abstract Accurate dynamical models of the Antarctic ice sheet with carefully specified initial conditions and well-calibrated rheological parameters are needed to forecast global sea level. By adapting an inverse method previously used in electric impedance tomography, we infer present-day flow speeds within the ice sheet. This inversion uses satellite observations of surface velocity, snow accumulation rate, and rate of change of surface elevation to estimate the basal drag coefficient and an ice stiffness parameter that influences viscosity. We represent interior ice motion using a vertically integrated approximation to incompressible Stokes flow. This model represents vertical shearing within the ice and membrane stresses caused by horizontal stretching and shearing. Combining observations and model, we recover marked geographical variations in the basal drag coefficient. Relative changes in basal shear stress are smaller. No simple sliding law adequately represents basal shear stress as a function of sliding speed. Low basal shear stress predominates in central East Antarctica, where thick insulating ice allows liquid water at the base to lubricate sliding. Higher shear stress occurs in coastal East Antarctica, where a frozen bed is more likely. Examining Thwaites glacier in more detail shows that the slowest sliding often coincides with elevated basal topography. Differences between our results and a similar adjoint-based inversion suggest that inversion or regularization methods can influence recovered parameters for slow sliding and finer scales; on broader scales we recover a similar pattern of low basal drag underneath major ice streams and extensive regions in East Antarctica that move by basal sliding.

1. Introduction

To predict how much Greenland and Antarctica will contribute to sea level rise, and how quickly, we must first develop ice sheet models that accurately represent the present-day flow of the ice. This motivates efforts to combine models of ice sheet flow with the many observations available from satellites, aircraft, and field campaigns [*Church et al.*, 2013; *Vaughan et al.*, 2013]. In Antarctica, these observations include measurements of surface elevation, bed elevation, surface velocity, snow accumulation rate, and the rate of change of surface elevation [e.g., *Le Brocq et al.*, 2010; *Fretwell et al.*, 2013; *Rignot et al.*, 2011; *Arthern et al.*, 2006; *Pritchard et al.*, 2009]. Here, using an inverse method described by *Arthern and Gudmundsson* [2010], we assimilate these observations into a class of ice flow model that allows efficient, depth-integrated approximations to Stokes flow to be applied in all areas of the ice sheet [*Goldberg*, 2011]. The assimilation of data into the model serves two purposes: first, it provides an initial state for the Antarctic ice flow model that can be used as a starting point for predictive modeling; second, it provides an analysis of the velocity at all depths within the ice, allowing us to investigate the factors that are controlling the ice flow.

The key reason for assimilating observations from satellites, aircraft, and field campaigns is that model predictions will only be useful if they are based on accurate information. This includes accurate initial conditions, boundary conditions, and parameters in the model. The important model parameters include the ice viscosity and the basal drag coefficient. The viscosity characterizes the resistance of the ice to deformation and may itself depend upon the rate of deformation if the rheology is nonlinear. The drag coefficient characterizes the slipperiness of the sediment or rock beneath the ice; the drag coefficient multiplied by the basal sliding speed gives the basal shear stress that acts to resist sliding. The drag coefficient may itself be a function of the basal sliding speed if the basal drag is nonlinear. Nonlinear drag laws can represent either resistance to flow around obstacles [*Weertman*, 1964], the lubricating influence of subglacial water-filled cavities [*Lliboutry*, 1968; *Fowler*, 2010], or the failure of subglacial sediment at a particular yield stress [*Bueler and Brown*, 2009; *Schoof*, 2010]. In addition to sliding speed, the drag coefficient may depend upon other spatially variable quantities, such as obstacle size or water pressure.

Both the viscosity and basal drag coefficient strongly influence how fast the ice flows. Together with the ice thickness, they control the flux of ice across the grounding line, where the ice goes afloat [*Schoof*, 2007]. They also determine how far and how fast perturbations at the coastal margins of the ice sheet can propagate into the interior [*Williams et al.*, 2012]. As a consequence, it is important to specify both the viscosity and basal drag coefficient accurately in simulations used to assess the stability of the ice sheet and to forecast its contribution to sea level rise. Accurate specification of the initial state and parameters is particularly important whenever small inaccuracies in the present state can become amplified as the forecast interval extends further and further into the future. This situation could arise if the ice sheet is dynamically unstable to perturbation, or close to a critical threshold where such an instability could take hold [*Schoof*, 2007; *Joughin et al.*, 2014].

The thickness of the ice sheet can reach several kilometers, but most of the available satellite observations do not identify quantities within its bulk, but at its upper surface. This raises the question of how the observations of the upper surface can be used to accurately infer the subsurface flow.

One way to obtain information from beneath the surface is to use inverse methods. In this approach, the basal drag coefficient, ice viscosity, or other parameters associated with ice flow beneath the surface are varied. These "control" parameters are adjusted until they attain optimal values that minimize the discrepancy between the predictions of the model and the observations at the upper surface. Since their introduction to glaciology by *MacAyeal* [1992] there has been ever increasing interest in using inverse methods to infer conditions at the base of the ice sheets, or deep within the ice. Satellites have assisted these advances by enabling widespread coverage of ice flow velocity [e.g., *Rignot et al.*, 2011], elevation changes [e.g., *Pritchard et al.*, 2009], and other surface observations.

A variety of approaches to invert for unknown parameters are now used in glaciology. Methods based on optimal control theory, often using adjoint equations, provide an efficient way to adjust model parameters so that the misfit with the observations is minimized [*MacAyeal*, 1992]. Rather than formulating the adjoint equations, automatic differentiation of computer programs can be used to derive the adjoint of the computer code that represents the model [*Heimbach and Bugnion*, 2009]. The optimal control theory approach can also be used when the observations are distributed through time [*Arthern and Hindmarsh*, 2003; *Goldberg and Heimbach*, 2013; *Larour et al.*, 2014]. Other methods in use include Bayesian estimation [*Berliner et al.*, 2008; *Raymond and Gudmundsson*, 2009], ensemble-based Monte Carlo methods [*Tarasov et al.*, 2012], and the ensemble Kalman filter [*Bonan et al.*, 2013]. A variety of iterative approaches to the inversion have also been developed [*Arthern and Gudmundsson*, 2010; *Pollard and DeConto*, 2012; *van Pelt et al.*, 2013].

Inverse methods have been used to infer basal drag coefficients [*MacAyeal*, 1992; *Vieli and Payne*, 2003; *Joughin et al.*, 2004] and the viscosity of floating ice shelves [*Rommelaere and MacAyeal*, 1997; *Larour et al.*, 2005; *Vieli et al.*, 2007; *Khazendar et al.*, 2007]. A complicating factor is the nonlinearity of the ice rheology and the nonlinearity of drag laws. Using surface data alone, it is difficult to uniquely identify many different parameters in a drag law without ambiguity, so inverse methods have tended to rely on very simple drag laws, rather than comprehensive modeling of the interactions of sediment and water within the subglacial environment. Nevertheless, the general approach of minimizing the misfit to observations has been used to characterize the non-Newtonian rheology of ice or sediment, or nonlinear sliding laws at the base of the ice [*Joughin et al.*, 2004; *Arthern and Gudmundsson*, 2010; *Jay-Allemand et al.*, 2011; *Petra et al.*, 2012].

Most of the early glaciological applications of inverse methods used simplified models appropriate for ice that is sliding over very slippery sediment or water [*Morland and Johnson*, 1980; *Muszynski and Birchfield*, 1987; *MacAyeal*, 1989]. This limited their application to floating ice shelves or ice streams. Ice shelves can be modeled as free slip on the lower boundary. Ice streams can be modeled as a special case of Navier slip [*Navier*, 1823], under a restrictive assumption that basal drag is low enough that the horizontal velocity varies little with depth [e.g., *MacAyeal*, 1989; *Joughin et al.*, 2004].

More recently, there has been a generalization of glaciological inverse methods to Stokes flow [*Maxwell et al.*, 2008; *Raymond and Gudmundsson*, 2009; *Arthern and Gudmundsson*, 2010; *Morlighem et al.*, 2010; *Schafer et al.*, 2012; *Gillet-Chaulet et al.*, 2012]. This has opened up the use of inversion for the whole range of basal drag conditions, and thus the entirety of the Antarctic and Greenland ice sheets.

Models of Stokes flow can be computationally expensive, so *Morlighem et al.* [2013] have applied optimal control methods, based upon adjoint equations, for a computationally cheaper approximation to Stokes flow in Antarctica [*Blatter*, 1995; *Pattyn*, 2002]. An even more efficient class of vertically integrated models has been

developed recently [*Hindmarsh*, 2004; *Bueler and Brown*, 2009; *Schoof and Hindmarsh*, 2010; *Goldberg*, 2011]. These models can be applied to both slippery and nonslippery basal conditions. Similar equations have been implemented by *Perego et al.* [2012] and *Cornford et al.* [2013]. These vertically integrated models represent the vertical profile of velocity implicitly, and the profile can be reconstructed explicitly if required. Thus, these approximations retain many of the advantages of the model considered by *Blatter* [1995], *Pattyn* [2002], and *Morlighem et al.* [2013], but they are even more efficient computationally. This efficiency has motivated us to apply one of them here to an inversion of the basal drag, viscosity, and three-dimensional velocity structure in Antarctica.

Although similar in overall concept, there are differences between this study and other recent inversions of basal drag in Antarctica [e.g., *Pollard and DeConto*, 2012; *Morlighem et al.*, 2013]. First, the system of equations we have used to describe the ice flow [see *Goldberg*, 2011] is different from these studies. Second, our approach to the inverse problem differs from the heuristic approach used by *Pollard and DeConto* [2012] and the adjoint-based approach used by *Morlighem et al.* [2013]. We apply an inverse method previously used for electric impedance tomography, a technique used in medical imaging and nondestructive testing, and demonstrate that this method can be applied to glaciology on a continental scale. Some background to the inverse method used to recover the basal drag coefficient and the ice viscosity is given in section 2. Third, we have made use of a wider variety of satellite observations, including the rate of snow accumulation and the rate of change of elevation from satellite altimetry, and this can provide information about ice flow even where the horizontal velocity has not been measured [*Williams et al.*, 2014; *Larour et al.*, 2014].

By simultaneously solving for the basal drag coefficient and the velocity at depths throughout the ice sheet, we can gain a better understanding of the processes operating within and underneath the Antarctic ice sheet. In particular, we can evaluate the success of different sliding parameterizations in explaining these geographical variations.

2. Background to the Inversion

Our algorithm is based on inverse methods developed for use in electric impedance tomography [*Calderon*, 1980; *Kohn and Vogelius*, 1984; *Chaabane and Jaoua*, 1999]. These methods are governed by the Laplace equation and allow structures internal to a body to be revealed from measurements of electric current and voltage on its outer surface. An analogous approach can be used to identify the drag coefficient and the ice viscosity when the ice flow is governed by the equations of incompressible Stokes flow [*Arthern and Gudmundsson*, 2010]. In this application it is not electrical measurements, but mechanical stresses and velocities that are known at the surface, and the viscosity and basal drag beneath the surface that are identified rather than the electric impedance. The main technical advance of this paper is to demonstrate that this method can also be applied to the vertically averaged approximation to Stokes flow used in our ice sheet model. Thus, the viscosity and basal drag coefficient can be recovered without the expense of solving the Stokes system.

As described by *Arthern and Gudmundsson* [2010] the inversion relies upon successive solutions of the momentum equations employed by the ice flow model. These provide the velocity field within the ice for any given geometry. The inversion is an iterative approach that minimizes a cost function representing the mismatch between the model and the data. At each iteration, incremental adjustments to the basal drag coefficient and the ice viscosity are made. To compute these adjustments, two separate velocity fields are evaluated. These correspond, respectively, to two alternate boundary conditions applied at the upper surface, first a Neumann (stress free) boundary condition and then a Dirichlet (prescribed velocity) boundary condition.

Solving first with Neumann then with Dirichlet boundary conditions allows the gradient of the cost function to be evaluated [see *Arthern and Gudmundsson*, 2010]. Once the gradient is available, this reveals how to adjust the basal drag coefficient and the ice viscosity to obtain a better agreement with the data at the next iteration. After multiple iterations the eventual result is that basal drag and viscosity are identified such that when the ice sheet model is run with a stress-free upper surface, it produces velocities that agree closely with the satellite observations.

A summary of the model equations for the Neumann problem is given in section 3. Section 4 specifies the Dirichlet problem for the given satellite measurements. For our vertically integrated model the application of Dirichlet boundary conditions at the upper surface is not as straightforward as it is for Stokes flow and requires

the approximate solution of a saddle-point problem. We emphasize that our labeling of the Neumann and Dirichlet problems refers specifically to the boundary condition on the upper surface, while other physically motivated boundary conditions apply at lateral and basal surfaces of the domain.

Section 5 presents expressions for the rates of heating caused by mechanical dissipation for both the Neumann solution and the Dirichlet solution. These expressions are used in the iterative scheme to solve for the basal drag coefficient β and the depth-averaged ice viscosity $\bar{\eta}$, as described in section 6. We defer all details of the numerical computations to a series of appendices in Text S1 in the supporting information. Results of the inversion are presented in section 8.

3. The Neumann Solution

To begin with, we give a brief overview of the equations used in the Neumann calculation. This is the standard ice sheet model. It has a stress-free upper boundary condition, as described by *Goldberg* [2011]. The model is a variation of a depth-integrated model analyzed by *Hindmarsh* [2004] and *Schoof and Hindmarsh* [2010]. Details of the derivation of these equations and the accuracy of the approximations employed are provided by *Goldberg* [2011] and *Schoof and Hindmarsh* [2010].

We use superscript N to identify quantities from the Neumann calculation. We use a Cartesian coordinate system x, y, and z (positive upward). The momentum conservation equations for the depth-averaged velocity components $\bar{u}^N(x, y)$ and $\bar{v}^N(x, y)$, in the x and y directions, respectively, are [*Goldberg*, 2011]

$$\partial_x \left[4\bar{\eta}h\partial_x\bar{u}^N + 2\bar{\eta}h\partial_y\bar{v}^N \right] + \partial_y \left[\bar{\eta}h\partial_x\bar{v}^N + \bar{\eta}h\partial_y\bar{u}^N \right] - \tau_{bx}^N = \rho_i gh\partial_x s \text{ and}$$

$$\partial_y \left[4\bar{\eta}h\partial_y\bar{v}^N + 2\bar{\eta}h\partial_x\bar{u}^N \right] + \partial_x \left[\bar{\eta}h\partial_y\bar{u}^N + \bar{\eta}h\partial_x\bar{v}^N \right] - \tau_{by}^N = \rho_i gh\partial_y s. \tag{1}$$

In these equations, ρ_i is the density of ice, g is gravitational acceleration, $\bar{\eta}(x, y)$ is depth-averaged viscosity, $h(x, y)$ is ice thickness, $s(x, y)$ is surface elevation, and τ_{bx}^N and τ_{by}^N are the basal drag in x and y directions.

The boundary conditions where the ice meets water at the lateral margin of the ice sheet are

$$-\frac{1}{2}\rho_w gh_w^2 \hat{n}_x = \int_b^s \sigma_{xx}^N \hat{n}_x + \sigma_{xy}^N \hat{n}_y \mathrm{d}z$$

$$= 2\bar{\eta}h(2\partial_x\bar{u}^N + \partial_y\bar{v}^N)\hat{n}_x - \frac{1}{2}\rho_i gh^2\hat{n}_x + \bar{\eta}h(\partial_y\bar{u}^N + \partial_x\bar{v}^N)\hat{n}_y \text{ and}$$

$$-\frac{1}{2}\rho_w gh_w^2 \hat{n}_y = \int_b^s \sigma_{yy}^N \hat{n}_y + \sigma_{xy}^N \hat{n}_x \mathrm{d}z$$

$$= 2\bar{\eta}h(2\partial_y\bar{v}^N + \partial_x\bar{u}^N)\hat{n}_y - \frac{1}{2}\rho_i gh^2\hat{n}_y + \bar{\eta}h(\partial_y\bar{u}^N + \partial_x\bar{v}^N)\hat{n}_x. \tag{2}$$

This assumes continuity of depth-integrated stress across the lateral boundary. The tensor components σ_{xx}^N, σ_{yy}^N, and σ_{xy}^N define stresses within the ice from extension in x and y directions and lateral shearing, respectively. The water density is ρ_w, and the ice draft (i.e., the thickness of ice beneath the water level) is $h_w(x, y)$, which may be zero for land-terminating sections of the margin. Assuming the water level lies at $z = 0$ we define $h_w = \max(h - s, 0)$. The water is assumed to be in hydrostatic equilibrium and exerts a normal stress on the boundary, but no shear stress. The x and y components of the unit vector normal to the lateral margin are n_x and n_y. The base of the ice is at $z = b(x, y)$. At lateral boundaries identified as rock, a no penetration condition is applied, so the ice must flow around mountains and nunataks.

Viscosity $\eta(x, y, z)$ is defined implicitly as follows [see *Goldberg*, 2011]:

$$\eta = \frac{1}{2}B \left[(\partial_x\bar{u}^N)^2 + (\partial_y\bar{v}^N)^2 + (\partial_x\bar{u}^N)(\partial_y\bar{v}^N) + \frac{1}{4}\left(\partial_y\bar{u}^N + \partial_x\bar{v}^N\right)^2 + \frac{1}{4}(\partial_z u^N)^2 + \frac{1}{4}(\partial_z v^N)^2 + \epsilon^2 \right]^{\frac{1-n}{2n}}, \tag{3}$$

in which $n = 3$ is the exponent in a nonlinear Glen flow law, $\epsilon = 10^{-5} \, \mathrm{a}^{-1}$ is a regularization parameter that imposes a transition to a linear rheology at small strain rate, and $B(x, y, z)$ is a temperature-dependent coefficient that determines the stiffness of the ice. For typical temperatures, the value $\epsilon = 10^{-5} \, \mathrm{a}^{-1}$ implies a transition to a linear rheology when effective stress drops to about 10 kPa, similar to the effective stress at which such a transition has been inferred near ice divides [*Pettit et al.*, 2011].

The reason that equation (3) is an implicit definition for viscosity η is that the strain rates for vertical shear themselves depend on viscosity. To the level of approximation used in the model, all horizontal gradients in vertical velocity w are neglected, so vertical shear can be approximated as

$$\partial_z u^N \approx \partial_z u^N + \partial_x w^N = \sigma_{xz}^N/\eta, \qquad \partial_z v^N \approx \partial_z v^N + \partial_y w^N = \sigma_{yz}^N/\eta. \tag{4}$$

Vertical shear stresses $\sigma_{xz}^N(x,y,z)$ and $\sigma_{yz}^N(x,y,z)$ are assumed to vary linearly with depth:

$$\sigma_{xz}^N = \tau_{bx}^N(s-z)/h \text{ and } \qquad \sigma_{yz}^N = \tau_{by}^N(s-z)/h. \tag{5}$$

Equation (3) includes the softening effects from vertical shearing and membrane stresses. For a nonlinear rheology with $n = 3$, the exponent takes the value $(1-n)/(2n) = -1/3$. In that case, given estimates of s, h, B, τ_{bx}^N, τ_{by}^N, $\partial_x \bar{u}^N$, $\partial_y \bar{u}^N$, $\partial_x \bar{v}^N$, and $\partial_y \bar{v}^N$, the viscosity η can be found by solving a cubic equation obtained by substituting equations (5) and (4) into equation (3) and rearranging. Integration over depth is then carried out by numerical quadrature to obtain the depth-averaged viscosity $\bar{\eta}(x,y)$,

$$\bar{\eta} = \frac{1}{h}\int_b^s \eta \, \mathrm{d}z. \tag{6}$$

Numerical quadrature can also be used to estimate some useful integrals $\mathcal{F}_\alpha(x,y)$ for $\alpha = 0$, 1, and 2, defined as follows:

$$\mathcal{F}_\alpha = \int_b^s \frac{1}{\eta}\left(\frac{s-z}{h}\right)^\alpha \mathrm{d}z. \tag{7}$$

A Robin (or Navier slip) boundary condition at the lower boundary linearly relates the basal drag τ_b^N to basal velocity $\boldsymbol{u}_b^N$ via a multiplicative drag coefficient β, so that

$$\tau_b^N = \beta \boldsymbol{u}_b^N, \tag{8}$$

with

$$\boldsymbol{u}_b^N(x,y) = \begin{bmatrix} u^N(x,y,b) \\ v^N(x,y,b) \end{bmatrix} \text{ and } \qquad \tau_b^N(x,y) = \begin{bmatrix} \tau_{bx}^N \\ \tau_{by}^N \end{bmatrix}. \tag{9}$$

Integrating equation (4) once to obtain the velocity as a function of depth and again to obtain the depth-integrated velocity, we obtain expressions for the surface velocity $\boldsymbol{u}_s^N(x,y)$,

$$\boldsymbol{u}_s^N(x,y) = \begin{bmatrix} u^N(x,y,s) \\ v^N(x,y,s) \end{bmatrix} = \boldsymbol{u}_b^N(1+\beta\mathcal{F}_1), \tag{10}$$

and the depth-averaged velocity,

$$\bar{\boldsymbol{u}}^N = \begin{bmatrix} \frac{1}{h}\int_b^s u^N(x,y,z)\mathrm{d}z \\ \frac{1}{h}\int_b^s v^N(x,y,z)\mathrm{d}z \end{bmatrix} = \boldsymbol{u}_b^N(1+\beta\mathcal{F}_2), \tag{11}$$

in which $\mathcal{F}_1$ and $\mathcal{F}_2$ are defined by equation (7). The effective drag coefficient β_{eff} is defined by *Goldberg* [2011] such that the basal drag $\tau_b^N = \beta_{\text{eff}}\bar{\boldsymbol{u}}^N$, giving

$$\beta_{\text{eff}} = \frac{\beta}{1+\beta\mathcal{F}_2}. \tag{12}$$

Sometimes it will be more convenient to use a shorthand notation for equation (1),

$$\mathcal{L}(\bar{\boldsymbol{u}}^N)\bar{\boldsymbol{u}}^N = \boldsymbol{f}, \tag{13}$$

in which

$$\mathcal{L} = \begin{bmatrix} \partial_x 4\bar{\eta}h\partial_x + \partial_y \bar{\eta}h\partial_y - \beta_{\text{eff}} & \partial_x 2\bar{\eta}h\partial_y + \partial_y \bar{\eta}h\partial_x \\ \partial_y 2\bar{\eta}h\partial_x + \partial_x \bar{\eta}h\partial_y & \partial_y 4\bar{\eta}h\partial_y + \partial_x \bar{\eta}h\partial_x - \beta_{\text{eff}} \end{bmatrix} \text{ and } \quad \boldsymbol{f} = \begin{bmatrix} \rho_i gh\partial_x s \\ \rho_i gh\partial_y s \end{bmatrix}. \tag{14}$$

A discretized finite difference approximation to equation (13) is described in Appendix A in Text S1. Because the depth-averaged viscosity $\bar{\eta}(x, y)$ depends on $\bar{u}^N(x, y)$ and $\bar{v}^N(x, y)$, equation (13) is nonlinear. Starting from an initial guess of $\bar{\eta}$ and β_{eff}, solving equation (13) to find $\bar{u}^N(x, y)$ and $\bar{v}^N(x, y)$ and then recomputing $\bar{\eta}$ and β_{eff} as described above forms the basis of an iterative method for solving equation (13). At each subsequent iteration $l = 2, 3, ...$, the operator $\mathcal{L}(\bar{\boldsymbol{u}}_{l-1}^N)$ is evaluated using $\bar{\boldsymbol{u}}_{l-1}^N$ derived at the previous iteration and equation (13) solved to provide a new estimate $\bar{\boldsymbol{u}}_l^N$. This cycle can be repeated until the norm of the residual of equation (13) is smaller than some tolerance, expressed as a fraction of the norm of $\boldsymbol{f}$.

For any depth-averaged velocity $\bar{\boldsymbol{u}}^N$, accumulation rate $a(x, y)$, and basal melt rate $m_b(x, y)$ the evolution of ice thickness h is given by

$$\partial_t h = a - m_b - \nabla \cdot (\bar{\boldsymbol{u}}^N h). \tag{15}$$

The rate of change of surface elevation is then

$$\partial_t s = \psi \partial_t h, \tag{16}$$

with $\psi(x, y) = 1$ for grounded ice, and $\psi(x, y) = (1 - \rho_i/\rho_w)$ for floating ice, to account for hydrostatic compensation. Equations (15) and (16) assume constant density ρ_i within the column but could be generalized by the addition of terms to account for the lower density of firn within the upper layers of the ice sheet and the possibility that this density varies over time [*Arthern et al.*, 2010].

4. The Dirichlet Solution

To use the algorithm described by *Arthern and Gudmundsson* [2010], we must be able to solve an analogous problem with velocity prescribed at the upper surface of the ice sheet as a Dirichlet boundary condition. In this section we describe the application of the Dirichlet boundary condition to the vertically integrated model. The momentum equations can be written in a more general form as

$$\partial_x \left[4\bar{\eta}h\partial_x\bar{u}^D + 2\bar{\eta}h\partial_y\bar{v}^D \right] + \partial_y \left[\bar{\eta}h\partial_x\bar{v}^D + \bar{\eta}h\partial_y\bar{u}^D \right] - \tau_{bx}^D + \tau_{sx}^D + h\partial_x\sigma_s^D = \rho_i gh\partial_x s \text{ and}$$
$$\partial_y \left[4\bar{\eta}h\partial_y\bar{v}^D + 2\bar{\eta}h\partial_x\bar{u}^D \right] + \partial_x \left[\bar{\eta}h\partial_y\bar{u}^D + \bar{\eta}h\partial_x\bar{v}^D \right] - \tau_{by}^D + \tau_{sy}^D + h\partial_y\sigma_s^D = \rho_i gh\partial_y s, \tag{17}$$

with lateral boundary conditions,

$$-\frac{1}{2}\rho_w gh_w^2\hat{n}_x = \int_b^s \sigma_{xx}^D\hat{n}_x + \sigma_{xy}^D\hat{n}_y \, \mathrm{d}z$$
$$= 2\bar{\eta}h \left(2\partial_x\bar{u}^D + \partial_y\bar{v}^D \right)\hat{n}_x - \frac{1}{2}\rho_i gh^2\hat{n}_x + \sigma_s^D h\hat{n}_x + \bar{\eta}h \left(\partial_y\bar{u}^D + \partial_x\bar{v}^D \right)\hat{n}_y \text{ and}$$
$$-\frac{1}{2}\rho_w gh_w^2\hat{n}_y = \int_b^s \sigma_{yy}^D\hat{n}_y + \sigma_{xy}^D\hat{n}_x \, \mathrm{d}z$$
$$= 2\bar{\eta}h \left(2\partial_y\bar{v}^D + \partial_x\bar{u}^D \right)\hat{n}_y - \frac{1}{2}\rho_i gh^2\hat{n}_y + \sigma_s^D h\hat{n}_y + \bar{\eta}h \left(\partial_y\bar{u}^D + \partial_x\bar{v}^D \right)\hat{n}_x. \tag{18}$$

As before, a no penetration condition is applied at mountains and nunataks. The main difference compared to the Neumann calculation outlined above is that in the Dirichlet solution the upper surface is no longer guaranteed to be stress free. Instead, the stress at the surface is that needed to satisfy the imposed Dirichlet boundary condition from the satellite data. In general, the Dirichlet solution therefore has a normal stress at the surface, which can be approximated for small slopes by

$$\sigma_s^D(x, y) = \sigma_{zz}^D(x, y, s), \tag{19}$$

and we also have both basal and surface shear stresses,

$$\boldsymbol{\tau}_b^D(x, y) = \begin{bmatrix} \tau_{bx}^D \\ \tau_{by}^D \end{bmatrix} \text{ and } \quad \boldsymbol{\tau}_s^D(x, y) = \begin{bmatrix} \tau_{sx}^D \\ \tau_{sy}^D \end{bmatrix}. \tag{20}$$

We retain the assumption that shear stress varies linearly with depth so that

$$\sigma_{xz}^D = \tau_{sx}^D + \left(\tau_{bx}^D - \tau_{sx}^D \right)(s - z)/h \text{ and}$$
$$\sigma_{yz}^D = \tau_{sy}^D + \left(\tau_{by}^D - \tau_{sy}^D \right)(s - z)/h. \tag{21}$$

Vertical shear is then approximated as

$$\partial_z u^D \approx \partial_z u^D + \partial_x w^D = \sigma_{xz}^D/\eta \quad \text{and} \quad \partial_z v^D \approx \partial_z v^D + \partial_y w^D = \sigma_{yz}^D/\eta. \tag{22}$$

We do not recompute viscosity $\eta(z)$ but simply reuse the viscosity field that was computed for the Neumann solution. This choice is somewhat heuristic but practically convenient. The rationale is that we are ultimately seeking to arrange that the Neumann solution, based on the Neumann viscosity, agrees with the Dirichlet solution, so forcing both simulations to have the same viscosity at intermediate steps during the inversion should not influence the final outcome. Additionally, it is the Neumann viscosity that is more relevant to any forward calculation using the model.

Integrating equation (22) once to obtain the velocity as a function of depth and again to obtain the depth-integrated velocity, we obtain

$$\boldsymbol{u}_s^D = \boldsymbol{u}_b^D(1 + \beta \mathcal{F}_1) + \boldsymbol{\tau}_s^D(\mathcal{F}_0 - \mathcal{F}_1) \quad \text{and}$$
$$\bar{\boldsymbol{u}}^D = \boldsymbol{u}_b^D(1 + \beta \mathcal{F}_2) + \boldsymbol{\tau}_s^D(\mathcal{F}_1 - \mathcal{F}_2), \tag{23}$$

in which $\mathcal{F}_1$ and $\mathcal{F}_2$ are defined by equation (7), and the basal and surface velocities are

$$\boldsymbol{u}_b^D(x, y) = \boldsymbol{u}^D(x, y, b) \quad \text{and} \qquad \boldsymbol{u}_s^D(x, y) = \boldsymbol{u}^D(x, y, s). \tag{24}$$

We have also used the basal boundary condition,

$$\boldsymbol{\tau}_b^D(x, y) = \beta \boldsymbol{u}_b^D, \tag{25}$$

to derive equations (23). Eliminating $\boldsymbol{u}_b^D$ from equations (23) gives the following expression for the surface velocity $\boldsymbol{u}_s^D$,

$$\boldsymbol{u}_s^D = \mathcal{R}\bar{\boldsymbol{u}}^D + \mathcal{P}\boldsymbol{\tau}_s^D, \tag{26}$$

in which

$$\mathcal{R} = \frac{1 + \beta \mathcal{F}_1}{1 + \beta \mathcal{F}_2} \quad \text{and}$$
$$\mathcal{P} = \mathcal{F}_0 - (\mathcal{R} + 1)\mathcal{F}_1 + \mathcal{R}\mathcal{F}_2. \tag{27}$$

Equations (23), (25), and (27) also allow the momentum equation (17) to be rewritten as follows:

$$\mathcal{L}(\bar{\boldsymbol{u}}^N)\bar{\boldsymbol{u}}^D - h\nabla(\rho_i gs - \sigma_s^D) + \mathcal{R}\boldsymbol{\tau}_s^D = 0. \tag{28}$$

We have written $\mathcal{L}(\bar{\boldsymbol{u}}^N)$ in equation (28) to emphasize that viscosity is derived from the Neumann calculation.

The data that we have available to prescribe the velocities at the surface consist of (i) the measured horizontal velocity $\boldsymbol{u}_s^*(x, y)$ at the surface of the ice sheet from satellite interferometric radar [*Rignot et al.*, 2011], (ii) the measured mass accumulation rate $a^*(x, y)$ [e.g., *Arthern et al.*, 2006], and (iii) the measured rate of change of surface elevation $\partial_t h^*(x, y)$ from satellite altimetry [*Wingham et al.*, 2006; *Pritchard et al.*, 2009]. For the Dirichlet simulation, the horizontal surface velocity is given by the observations, so we impose

$$\boldsymbol{u}_s^D = \boldsymbol{u}_s^* \tag{29}$$

as a constraint. Also, from mass conservation, the horizontal divergence of the ice flux for grounded ice is

$$\nabla \cdot (\bar{\boldsymbol{u}}^D h) = a^* - \partial_t h^*, \tag{30}$$

which provides a further constraint on the Dirichlet solution. A discrete finite difference approximation of equations (28), (26), (29), and (30) with boundary conditions (18) is described in Appendix A in Text S1. The discretized system takes the form of a saddle-point problem [*Benzi et al.*, 2005].

5. Heating Rates

To apply the algorithm described by *Arthern and Gudmundsson* [2010] for the vertically integrated model, it is convenient to evaluate the depth-integrated heating rates per unit area $Q_f(x, y)$ caused by frictional heating at the base and $Q_i(x, y)$ from internal deformation. The internal heating rate $Q_i(x, y)$ is the sum of heating $Q_v(x, y)$ caused by vertical shearing in the ice and $Q_m(x, y)$ caused by membrane stresses from lateral extension compression and shearing. To the level of approximation used by the forward model, these are

$$Q_f^N = \beta \left| \boldsymbol{u}_b^N \right|^2,$$

$$Q_i^N = \int_b^s 2\eta \left| \boldsymbol{e}^N \right|_F^2 dz = Q_v^N + Q_m^N,$$

$$Q_v^N \approx \int_b^s \eta \left| \partial_z \boldsymbol{u}^N \right|^2 dz = \left| \tau_b^N \right|^2 \mathcal{F}_2, \text{ and}$$

$$Q_m^N \approx \bar{\eta} h \left[4(\partial_x \bar{u}^N)^2 + 4(\partial_y \bar{v}^N)^2 + 4(\partial_x \bar{u}^N)(\partial_y \bar{v}^N) + (\partial_y \bar{u}^N + \partial_x \bar{v}^N)^2 \right].$$

(31)

For the Dirichlet solution, the heating rates are approximated as follows:

$$Q_f^D = \beta \left| \boldsymbol{u}_b^D \right|^2,$$

$$Q_i^D = \int_b^s 2\eta \left| \boldsymbol{e}^D \right|_F^2 dz = Q_v^D + Q_m^D,$$

$$Q_v^D \approx \int_b^s \eta \left| \partial_z \boldsymbol{u}^D \right|^2 dz = \left| \tau_s^D \right|^2 \mathcal{F}_0 + 2\tau_s^D.(\tau_b^D - \tau_s^D)\mathcal{F}_1 + \left| \tau_s^D - \tau_b^D \right|^2 \mathcal{F}_2, \text{ and}$$

$$Q_m^D \approx \bar{\eta} h \left[4(\partial_x \bar{u}^D)^2 + 4(\partial_y \bar{v}^D)^2 + 4(\partial_x \bar{u}^D)(\partial_y \bar{v}^D) + (\partial_y \bar{u}^D + \partial_x \bar{v}^D)^2 \right].$$

(32)

In these equations, $\left| \boldsymbol{e}^N \right|_F$ and $\left| \boldsymbol{e}^D \right|_F$ are the Frobenius norms of the strain rate tensors from the Neumann and Dirichlet simulations, respectively, and $\left| \boldsymbol{u}_b^N \right|$ and $\left| \boldsymbol{u}_b^D \right|$ are the magnitudes of the basal velocities. Similar notation is used for the magnitude of stresses $\left| \tau_b^N \right|$, $\left| \tau_b^D \right|$, etc.

6. Inversion for the Basal Drag Coefficient and Ice Stiffness

We solve for the basal drag coefficient β and the ice stiffness coefficient B that controls the viscosity using the algorithm described by *Arthern and Gudmundsson* [2010], which iteratively minimizes the Kohn and Vogelius cost function $J_{KV}(\eta, \beta)$,

$$J_{KV} = \int_\Omega 2\eta \left| \boldsymbol{e}^D - \boldsymbol{e}^N \right|_F^2 dV + \int_{\Gamma_b} \beta \left| \boldsymbol{u}^D - \boldsymbol{u}^N \right|^2 dS.$$

(33)

In equation (33) the volume integration is over the ice volume Ω and the surface integration is over the base of the ice sheet Γ_b. This cost function represents the mismatch between the Neumann and Dirichlet velocity fields (it can be viewed in abstract as the heat that would be dissipated by a hypothetical flow field obtained by subtracting the two velocity fields). Expressions from *Arthern and Gudmundsson* [2010] provide the gradient of this cost function, and an iterative algorithm for its minimization. At each iteration, the Neumann and Dirichlet problems were solved numerically as described in Appendix A in Text S1, and the heating rates evaluated using expressions in section 5 and Appendix D in Text S1.

The basal drag coefficient was updated as follows:

$$\beta_{n+1}(x, y) = \beta_n(x, y) + \alpha_\beta \left(\left| \boldsymbol{u}_b^N \right|^2 - \left| \boldsymbol{u}_b^D \right|^2 \right),$$

(34)

where α_β is a positive parameter that determines the step size. Using a constant α_β would correspond to minimization by a steepest descent method. However, following *Schafer et al.* [2012], a convenient alternative choice is

$$\alpha_\beta = \frac{\beta_n}{\left| \boldsymbol{u}_b^D \right|^p} \frac{\left(\left| \boldsymbol{u}_b^N \right|^p - \left| \boldsymbol{u}_b^D \right|^p \right)}{\left(\left| \boldsymbol{u}_b^N \right|^2 - \left| \boldsymbol{u}_b^D \right|^2 \right)}.$$

(35)

This quantity is positive everywhere, and for finite $\left|\mathbf{u}_b^D\right|$ can be made arbitrarily small as $p \to 0$. The reason for this choice is that the update to β can be written simply as

$$\beta_{n+1}(x,y) = \beta_n(x,y) \left(\frac{Q_f^N(x,y)}{Q_f^D(x,y)} \right)^p. \tag{36}$$

The initial guess $\beta_0(x,y)$ was set to 1×10^{-4} Pa m s^{-1} for floating ice and 1×10^4 Pa m s^{-1} for grounded ice, and we used $p = 0.1$.

Arthern and Gudmundsson [2010] also provide the following rule for updating the viscosity

$$\eta_{n+1}(x,y,z) = \eta_n(x,y,z) + \alpha_\eta \left(\left|\mathbf{e}^N\right|_F^2 - \left|\mathbf{e}^D\right|_F^2 \right), \tag{37}$$

where α_η is a positive parameter that determines the step size. We choose

$$\alpha_\eta = \frac{2h\eta_n(x,y,z)\bar{\eta}_n(x,y)}{\left(Q_i^D\right)^q} \left[\frac{\left(Q_i^N\right)^q - \left(Q_i^D\right)^q}{\left(Q_i^N\right) - \left(Q_i^D\right)} \right], \tag{38}$$

which is positive everywhere, and for finite Q_i^D can be made arbitrarily small as $q \to 0$. Integrating equation (37) with respect to depth then gives

$$\bar{\eta}_{n+1}(x,y) = \bar{\eta}_n(x,y) \left(\frac{Q_i^N(x,y)}{Q_i^D(x,y)} \right)^q. \tag{39}$$

Strictly, this applies only for a linear rheology. Nevertheless, at each iteration, we updated the ice stiffness coefficient $B(x,y,z)$ heuristically as follows:

$$B_{n+1}(x,y,z) = B_n(x,y,z) \left(\frac{Q_i^N(x,y)}{Q_i^D(x,y)} \right)^q. \tag{40}$$

The initial guess $B_0(x,y,z)$ was derived from ice temperatures $T(x,y,z)$ [*Pattyn*, 2010] using temperature sensitivity from *Paterson* [1994],

$$B_0 = A_0^{-\frac{1}{n}} \quad \text{and} \quad A_0 = A_{\text{ref}} e^{-E_A \left(\frac{1}{RT} - \frac{1}{RT_{\text{ref}}} \right)}, \tag{41}$$

with $n = 3$, $A_{\text{ref}} = 1.55 \times 10^{-17}$ Pa^{-n} yr^{-1}, $E_A = 58{,}600$ J mol^{-1}, $R = 8.314$ J mol^{-1} K^{-1}, $T_{\text{ref}} = 263$ K. A value $q = 0.1$ was used for ice shelves.

When the ice is grounded, simultaneous estimation of viscosity and drag coefficient is ill posed, and prior information is needed to regularize the problem [*Arthern and Gudmundsson*, 2010]. One way of introducing prior information is to select a value of q such that B departs from the initial guess B_0 only by an amount consistent with some assumed prior uncertainty. We experimented with three different values $q = [0, 0.01, 0.1]$. For $q = 0$ viscosity on the grounded ice was not updated at all, so only the drag coefficient was estimated. For $q = 0.1$ we observed that B differed from the initial guess B_0 in places by 5 orders of magnitude. For $q = 0.01$ estimates of B on grounded ice remained roughly within an order of magnitude of the initial guess B_0.

There is some ambiguity to the recovered values of B on grounded ice, and it is difficult to be precise about prior uncertainty in B, but, given the uncertainties in temperature, ice-damage, crystal fabric, grain size, and impurity content, an order of magnitude uncertainty in B seems possible. We therefore used $q = 0.01$ on grounded ice for the results presented in section 8. This allows some adjustment of the B away from the initial estimate B_0, while remaining consistent with a prior judgment of an order of magnitude uncertainty in that estimate. We make some further remarks about this procedure in section 8.
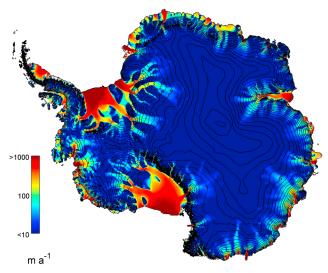
Figure 1. The flow speed at the upper surface from the ice sheet model after assimilation of satellite observations and inversion for basal drag coefficient and viscosity.

7. Surface Relaxation

Appendix E in Text S1 describes a numerical scheme for evolving the geometry of the surface, based on the equations for continuity (15) and surface elevation change (16). This requires many solutions of the Neumann problem to evaluate the velocities at each time step, and we found it useful to use an iterative approach with a multilevel, wavelet-based preconditioner inspired by *Vasilyev and Kevlahan* [2005]. This approach uses a basis of lifted wavelets to approximate the velocity field [*Sweldens*, 1998]. This wavelet decomposition is used to define an adaptive grid that can represent the velocity field without wasting computational effort in regions where the velocity field is smooth. Further details are provided in Appendices F and G in Text S1. We used this approach to investigate the sensitivity to relaxing the surface of the ice sheet [e.g., *Gillet-Chaulet et al.*, 2012]. For simulations with surface relaxation, we applied an adjusted accumulation rate of $a_{relax} = a^* - \partial_t h^*$ for a set period of time (2000 years) and then reverted to the observed accumulation rate a^*. For the grounded portion of the ice sheet the basal melt rate $m_b(x, y)$ was assumed negligible. The thickness of floating ice shelves was not altered. The surface relaxation brings the flux divergence into much better agreement with the observations of accumulation rate a^* and rate of elevation change $\partial_t h^*$. The price paid for this agreement is that the surface elevation and horizontal velocities agree less well with the satellite observations. Results before and after surface relaxation are presented below.

8. Results and Discussion

We solved for the basal drag coefficient β and ice stiffness B in Antarctica using the methods described above. Various data sets were used in this inversion: ice thickness, surface elevation, and bed elevation at 5 km grid spacing from the ALBMAP data set [*Le Brocq et al.*, 2010]; snow accumulation rates from *Arthern et al.* [2006]; rate of change of surface elevation from satellite laser altimetry [*Pritchard et al.*, 2009] and radar altimetry above 2000 m elevation in East Antarctica [*Wingham et al.*, 2006]; internal ice temperatures from *Pattyn* [2010]; and horizontal flow velocities from *Rignot et al.* [2011]. The 5 km ALBMAP grid spacing defined the model resolution.

Figure 1 shows the horizontal speed at the upper surface of the ice sheet from the Neumann solution. This is the standard ice flow model with a stress-free upper surface. The inversion has allowed many features of Antarctic ice flow to be represented in the model, including the fast-flowing ice streams and the rapid flow of ice shelves. The model gives a spatially continuous representation of the ice flow in Antarctica.
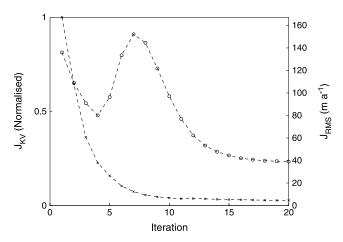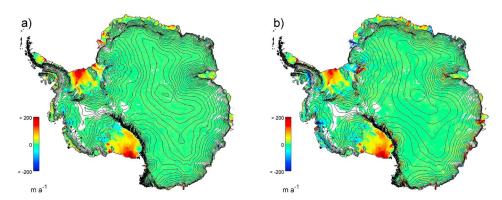

Figure 2. Changes in the cost function J_{KV} (crosses, left scale) and the root-mean-square discrepancy between data and model velocity at the surface (circles, right scale). Values are shown for each iteration during the inversion.

Figure 3. The difference between the model velocities and the satellite velocity observations: (a) before surface relaxation and (b) after surface relaxation. White areas have no valid data for the comparison.

The use of observations of accumulation rate and the rate of change of elevation provides information, even where the horizontal velocities are not measured [*Williams et al.*, 2014].

Figure 2 shows the iteration by iteration reduction of the cost function. The variation in root-mean-square (RMS) discrepancy between the model surface velocities and the satellite observations is shown on the same plot. There are points during the inversion where the RMS mismatch is increasing while the Kohn and Vogelius cost function is decreasing, then the RMS mismatch reduces again until both the cost function and the RMS discrepancy finally reach a level at which they stagnate. A similar stagnation has previously been seen for synthetic noisy observations [*Arthern and Gudmundsson*, 2010].

Figure 3 shows the mismatch between the horizontal speed from the model and the satellite measurements after 20 iterations. There are some locations where a mismatch persists; but, as would be expected for a successful inversion, the percentage mismatch in flow velocity is generally small. The greatest differences are seen on the ice shelves. Figure 4 shows the mismatch for the rate of elevation change. Here the greatest mismatches are seen on fast-flowing ice. The comparison was not performed for regions shown white in Figures 3 and 4, either because they are floating or because they have no satellite data. Figures 5 and 6 show histograms of the mismatch which show the magnitude of the mismatches before and after surface relaxation more clearly. Figure 6 shows that the mismatch in the rate of elevation change is substantially reduced after applying the surface relaxation.

Figure 7 shows the fields of basal drag coefficient recovered using the inverse method described above. The lowest values for the drag coefficient correspond to regions where the underlying sediment is slippery. These values can be compared to those recovered by *Morlighem et al.* [2013] who plot values of the square root of drag coefficient β. To assist comparison with results of *Morlighem et al.* [2013], we also provide a plot of the square root of β in Figure S1 in the supporting information. Our values of β are slightly higher in central regions of East Antarctica, but mainly where the sliding speed is anyway very small. Our values exhibit more spatial variability from place to place, which may reflect differences in the inversion method, or in the approach to
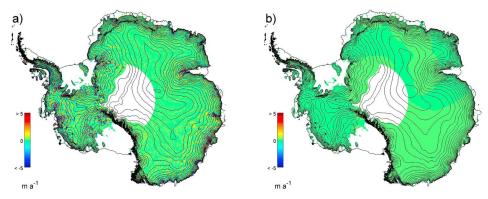

Figure 4. The difference between the model and the satellite observations of the rate of elevation change: (a) before surface relaxation and (b) after surface relaxation. White areas have no valid data for the comparison.
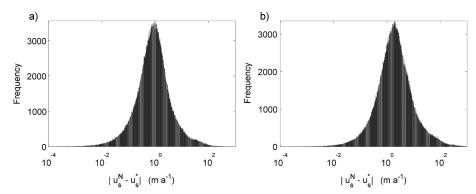
Figure 5. Histogram of the absolute difference between the model velocities and the satellite velocity observations on a logarithmic scale: (a) before surface relaxation and (b) after surface relaxation.

regularization. On the faster sliding ice streams we recover values below 100 Pa m^{-1} a, with a spatial pattern very similar to that identified by *Morlighem et al.* [2013].

It is worth emphasizing that although we invert for the drag coefficient β in a linear sliding law, this drag coefficient β could itself be a function of the local sliding velocity if the sliding law is nonlinear. To test whether geographical variations lend any support for a nonlinear sliding law, we plot the basal drag coefficient against basal sliding speed on a logarithmic scale (Figure 8). The basal drag coefficient can change by a factor of 10^{10} depending upon location. Contours of the basal shear stress (the product of the drag coefficient and the basal sliding speed) are also shown in Figure 8. If all the plotted data lay precisely along one of these contours, then basal drag could be characterized by specifying a uniform basal shear stress, which would simplify modeling [e.g., *Bueler and Brown*, 2009; *Schoof*, 2010]. At first glance the glaciological rule of thumb that basal shear stress is roughly 1 bar or 100 kPa has some merit. Even so, the basal shear stress varies by more than 3 orders of magnitude from less than 1 kPa to more than 1 MPa, so the basal drag cannot be represented well either by a uniform drag coefficient or by a uniform yield stress throughout Antarctica.

The geographical variations in basal shear stress are shown in Figure 9. There is a general pattern of higher basal shear stress around the margins of East Antarctica and lower values in the interior. In central East Antarctica, the ice is thick enough to insulate the ice and geothermal heating allows the basal temperature to reach the pressure melting point [*Pattyn*, 2010]. The water produced acts to lubricate the base of the ice sheet, lowering basal shear stress. As an example, low basal shear stress is recovered at the location of Lake Vostok in East Antarctica, where the ice is known to be afloat. Nearer the margins the ice is thinner, and it is more likely that the ice sheet is frozen to its base [*Pattyn*, 2010], producing high basal shear stress. In West Antarctica, the basal shear stress is low for ice streams that are known to be underlain by water-saturated sediment [e.g., *Vogel et al.*, 2005].

Figure 10 shows the basal shear stress normalized by the ice overburden $\rho_i g h$, plotted against a nondimensionalized sliding velocity u_b/u^*, where $u^* = l^* B_b^{-n}(\rho_i g h)^n$, with ice stiffness at the bed B_b from our inversion, and $l^* = 1$ m. A simple nonlinear sliding law as proposed by *Weertman* [1964] would appear in Figure 10 as
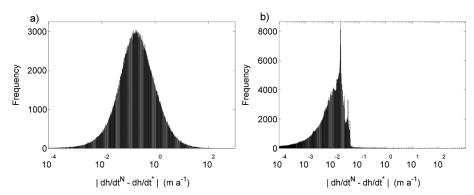

Figure 6. Histogram of the absolute difference between the model and the satellite observations of the rate of elevation change on a logarithmic scale: (a) before surface relaxation and (b) after surface relaxation.
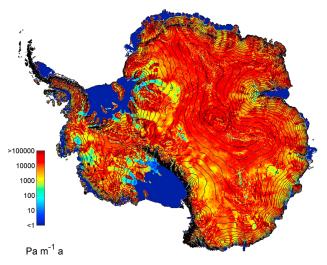
Figure 7. The basal drag coefficient in Antarctica from the inversion.

a straight line if factors such as obstacle size and spacing were assumed uniform throughout Antarctica. The scatter in Figure 10 shows that such a simple polynomial sliding law cannot represent basal drag in Antarctica unless geographical variation in the geometry or spacing of controlling obstacles is allowed.

Theories of subglacial cavitation [*Lliboutry*, 1968; *Schoof*, 2005; *Fowler*, 2010] predict that basal shear stress τ_b should not only be a function of basal sliding velocity u_b but should also depend on the basal water pressure p_w. A theoretical investigation of cavitation led *Schoof* [2005] to propose a drag law that can be written as

$$\frac{\tau_b}{\rho_i gh} = C[r^{-n} + \frac{u^*}{u_b}]^{-1/n}, \qquad (42)$$

where drag τ_b acts in the opposite direction to the sliding velocity u_b, $u^* = l^* B_b^{-n}(\rho_i gh)^n$ is a velocity scale, l^* is a length scale associated with cavity depth, C is a dimensionless constant smaller than the maximum bed slope, and $r = N/(\rho_i gh)$ is the ratio of effective pressure defined by $N = \rho_i gh - p_w$ to the ice overburden $\rho_i gh$. If we assume that points near the upper envelope of our observations have sufficiently low water pressure that the effective pressure is approximately equal to the overburden, so that $r \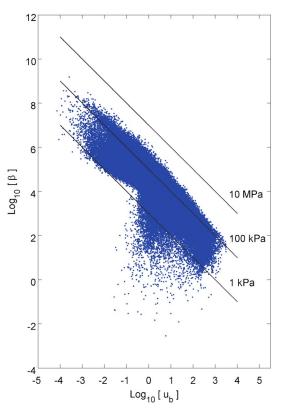approx 1$ [cf. *Jay-Allemand et al.*, 2011], then our results are approximately consistent with a sliding law of the form (42), with $l^* = 1$ m and $C = 1$. Contours of r derived using these values are plotted. Values from grid cells where subglacial lakes have been identified by *Wright and Siegert* [2012] are plotted in red. These generally correspond to low values of r predicted by the theory, as would be expected for ice that is floating or very close to floatation. Based on these contours, many locations in Antarctica not identified as subglacial lakes are also predicted to have low effective pressure, close to floatation, provided that $l^* = 1$ m and $C = 1$ are taken as representative values. We should point out though that in addition to variations in r, geographical variation in the parameters l^* and C might also be expected, so these results do not uniquely constrain the basal water pressure. Nevertheless, from theory and observations it seems likely that variations in the effective pressure could be responsible for much of the geographical variation in basal shear stress shown in Figure 9.

In summary, the geographical variations in slipperiness from our inversion are not represented well by a linear sliding law, a Weertman sliding law, or a uniform yield stress, unless geographical variations in parameters are allowed. There is evidence that variation in subglacial water pressure may control these geographical variations. Better
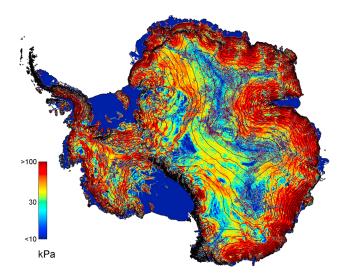

Figure 8. The basal drag coefficient from the inversion plotted against sliding velocity at the bed on a logarithmic scale.

Figure 9. The basal shear stress in Antarctica from the inversion.

models of the subglacial hydrological system, and independent information about the geometry of the bed, will be needed to physically characterize all the factors controlling basal drag without ambiguity. In the meantime, simplified models of basal drag calibrated using inverse methods represent a clear advance over simple sliding laws with geographically uniform coefficients. Furthermore, these inverse methods presently provide the only spatially distributed estimates of basal drag and basal velocity that are suitable for testing more complicated models of the subglacial environment.

Figure 11 shows the ratio of horizontal flow speed at the bed to horizontal flow speed at the upper surface. Values close to unity give an indication of where the ice sheet is sliding freely over water or slippery sediment with little vertical shearing within the ice. This is generally the case for fast-flowing ice streams, but the ratio also approaches unity in parts of East Antarctica, revealing regions there where the motion in is dominated by sliding. Lower values indicate stronger vertical shearing within the ice. On broad scales, similar features to those recovered by *Morlighem et al.* [2013] and *Sergienko et al.* [2014] are seen in this map. The locations of the subglacial lakes identified by *Wright and Siegert* [2012] are also shown on this plot.

Figure 12 shows the depth-averaged ice viscosity from the inversion. As mentioned above, values of ice stiffness B on grounded ice were allowed to vary within an order of magnitude of the initial guess by selecting a particular value for the step-size parameter q. The results shown are for a value of $q = 0.01$. We have not assumed that ice stiffness is known perfectly on the grounded ice because this seems likely to overestimate the ice stiffness in shear margins where ice becomes damaged. Allowing ice stiffness B to depart from the initial guess on grounded ice may also compensate for errors caused by uncertainty in ice temperatures.

Varying q on grounded ice while keeping p fixed alters the relative tendency to adjust either B or β during the inversion. For the same number of iterations a smaller value for the step-size parameter q, such as $q = 0.001$, would constrain the ice stiffness B to be closer to the initial guess B_0 and compensating changes would then be made to the basal drag coefficient β. On the floating ice shelves the basal drag can be assumed negligible, so these viscosities can be estimated more reliably than those on grounded ice. The inversion allows the model to represent damaged zones produced by shearing at the margins of floating ice shelves.

Figure 13 shows a higher-resolution example of our inversion applied to Bedmap2 data for the surface elevation and ice thickness [*Fretwell et al.*, 2013]. This limited-area inversion covers Pine Island and Thwaites and Smith glaciers
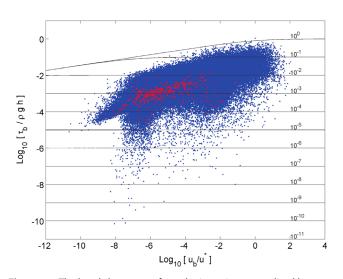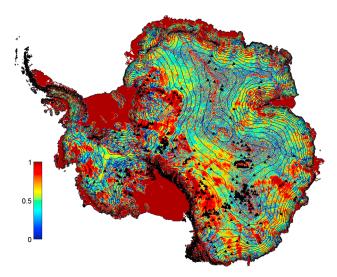

Figure 10. The basal shear stress from the inversion, normalized by overburden pressure and plotted against nondimensional sliding velocity at the bed on a logarithmic scale. Contours of r, the ratio of effective pressure to overburden, predicted by a theory of cavitation [*Schoof*, 2005] are shown. Values from grid cells where subglacial lakes have been observed by *Wright and Siegert* [2012] are shown in red.

Figure 11. The ratio of flow speed at the bed to flow speed at the surface of the ice sheet. Triangles show subglacial lakes identified by *Wright and Siegert* [2012].

and was performed at a higher resolution of 2 km. A zero-flow constraint was applied at the ice divide. Movie S1 in the supporting information shows multiple slices through the ice, revealing the complex velocity structure in this region. Where the flow speed is fastest, it does not change much between surface and the bed. In these regions, models that neglect vertical shearing [e.g., *Joughin et al.*, 2014] should give reliable results. However, the fast-sliding regions are interleaved with regions of slower sliding. These often coincide with high points in the bed elevation, possibly because thinner ice provides less insulation and the bed remains frozen. Alternatively, basal topography might affect the subglacial hydrology or availability of sediment. To model the evolution of the entire ice sheet will require models (as described by this study or *Goldberg*, [2011]) that can represent vertical shearing in the slowly sliding regions as well as stretching and lateral shearing where sliding is fast.

9. Conclusions and Further Developments

By using inverse methods, we have estimated the basal drag coefficient and the ice stiffness in Antarctica. These are key parameters needed to initialize forecasts of how the ice sheet will evolve in future. Our motivation is to provide more realistic dynamical simulations of how the ice sheet changes over time and improve forecasts of the contribution that Antarctica will make to global sea level.

We have shown that an algorithm originally developed for electric impedance tomography [*Kohn and Vogelius*, 1984; *Chaabane and Jaoua*, 1999] and adapted to Stokes flow [*Arthern and Gudmundsson*, 2010] can be used with vertically integrated models [*Goldberg*, 2011] to invert for the basal drag coefficient and the viscosity of the ice.

The basal drag coefficient is extremely variable from place to place. Our recovered values change by factors exceeding 10^{10} depending upon location. The relative varia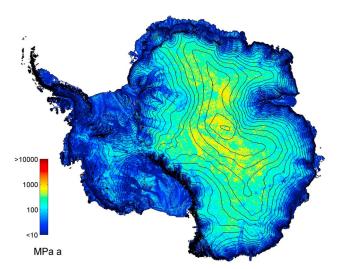tions in basal shear stress are smaller. However, no simple sliding law prescribing basal shear stress as a function of basal velocity is able to represent its variations.

In general, basal shear stress is lower in central East Antarctica, and close to previously identified subglacial lakes, where thermal insulation by thick ice allows the basal ice to reach the pressure melting point. This is consistent with theories of cavitation that predict that subglacial water pressure should provide an important control on basal drag. Basal shear stress is higher in coastal East Antarctica where basal ice is more likely to be frozen [*Pattyn*, 2010].

Our recovered velocities support the finding that extensive regions in East Antarctica move by basal sliding rather
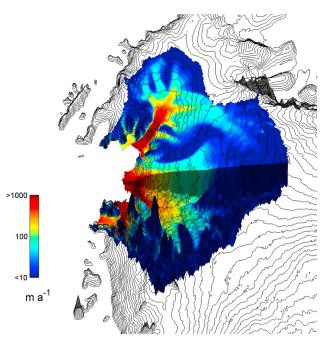

Figure 12. Depth-averaged viscosity in Antarctica from the inversion.

Figure 13. A cutaway three-dimensional view through Thwaites glacier showing flow speeds. The upper half of the cutaway figure shows the surface flow speed plotted at the level of the surface elevation. The lower half shows the basal sliding speed plotted at the basal elevation. Regions of slow basal sliding often correspond to regions where the bed is elevated. Contours at 100 m intervals indicate surface elevation. A vertical slice through Thwaites glacier (shaded) illustrates how the ice thickens toward the interior of the ice sheet.

than internal deformation [cf. *Morlighem et al.*, 2013; *Sergienko et al.*, 2014]. On broad scales our approach recovers basal drag coefficients similar to an adjoint-based method [*Morlighem et al.*, 2013]. There are differences on finer scales, and these may be related either to the differences in the inverse methods used, differences in the models, or differences in the approaches to regularizing the inversion.

Additional work will be needed to fully characterize the state of the ice sheet without ambiguity. This applies especially to the regularization of the inversion, which can affect the recovery of features at short spatial scales, and to the simultaneous inversion of basal drag coefficient and ice viscosity on grounded ice, so that damaged zones in the shear margins of ice streams can be represented. Since the available data do not allow unique determination of basal drag and viscosity on grounded ice without additional assumptions, and since these parameters will affect the forecast of the ice flow in any forward simulation, it will be important to explore different ways of regularizing this ill posedness, and the consequences that this has for simulations of the future.

The approaches described here could be developed further. The higher-resolution inversion using Bedmap2 data shown in Figure 13 could be repeated elsewhere in Antarctica. The internal ice temperatures from *Pattyn* [2010] provide a reasonable estimate of temperatures, but a more consistent procedure would be to solve for temperatures using the exact velocity field that we derive from the inversion. Even then, uncertainty in the geothermal heating would mean that temperatures are uncertain. More recent satellite altimetry from CryoSat-2 [*McMillan et al.*, 2014] could also be introduced. As the length of time spanned by the instrumental record becomes longer, it will become important to include the temporal dimension in the initialization procedure [e.g., *Goldberg and Heimbach*, 2013; *Larour et al.*, 2014].

The results of our inversion provide insight into the flow of the Antarctic ice sheet. They highlight the importance of the subglacial hydrology and the thermal regime in controlling basal drag in Antarctica. It seems possible that basal shear stress could vary in time if the basal water pressure responds to subglacial lake drainage or rearrangement of the hydrological system, so efforts to model the subglacial hydrology in Antarctica and how it evolves may become increasingly important. In West Antarctica, the association between regions of slow basal sliding and regions where the bed is elevated suggests that the influence of the underlying topography on the thermal or hydrological regime is an important factor in controlling the basal drag. The relative importance of thermal and hydrological controls on these variations in sliding merits further investigation. The information about the basal sliding from our inversions would assist such studies.

References

Arthern, R., and R. Hindmarsh (2003), Optimal estimation of changes in the mass of ice sheets, *J. Geophys. Res.*, *108*(F1), 6007, doi:10.1029/2003JF000021.

Arthern, R., D. Winebrenner, and D. Vaughan (2006), Antarctic snow accumulation mapped using polarization of 4.3-cm wavelength microwave emission, *J. Geophys. Res.*, *111*, D06107, doi:10.1029/2004JD005667.

Arthern, R. J., and G. H. Gudmundsson (2010), Initialization of ice-sheet forecasts viewed as an inverse Robin problem, *J. Glaciol.*, *56*(197), 527–533.

Arthern, R. J., D. G. Vaughan, A. M. Rankin, R. Mulvaney, and E. R. Thomas (2010), In-situ measurements of Antarctic snow compaction, compared with predictions of models, *J. Geophys. Res.*, *115*, F03011, doi:10.1029/2009JF001306.

Benzi, M., G. H. Golub, and J. Liesen (2005), Numerical solution of saddle point problems, *Acta Numerica*, *14*, 1–137, doi:10.1017/S0962492904000212.

Berliner, L. M., K. Jezek, N. Cressie, Y. Kim, C. Q. Lam, and Q. Van der Veen (2008), Modeling dynamic controls on ice streams: A Bayesian statistical approach, *J. Glaciol.*, *54*(187), 705–714, doi:10.3189/002214308786570917.

Blatter, H. (1995), Velocity and stress-fields in grounded glaciers—A simple algorithm for including deviatoric stress gradients, *J. Glaciol.*, *41*(138), 333–344.

Bonan, B., M. Nodet, C. Ritz, and V. Peyaud (2013), An ETKF approach for initial state and parameter estimation in ice sheet modelling, *Nonlinear Processes Geophys.*, *21*, 569–582, doi:10.5194/npg-21-569-2014.

Bueler, E., and J. Brown (2009), Shallow shelf approximation as a "sliding law" in a thermomechanically coupled ice sheet model, *J. Geophys. Res.*, *114*, F03008, doi:10.1029/2008JF001179.

Calderon, A. P. (1980), On an inverse boundary value problem, in *Seminar on Numerical Analysis and Its Applications to Continuum Physics, Rio de Janeiro*, edited by W. Meyer and M. Raupp, pp. 65–73, Soc Brasileira Matematica Aplicada and Computacional, Sao Carlos, Brazil.

Chaabane, S., and M. Jaoua (1999), Identification of Robin coefficients by the means of boundary measurements, *Inverse Prob.*, *15*(6), 1425–1438.

Church, J., et al. (2013), Sea level change, in *Climate Change 2013: The Physical Science Basis. Contribution of Working Group I to the Fifth Assessment Report of the Intergovernmental Panel on Climate Change*, edited by T. F. Stocker, chap. 13, pp. 1137–1216, Cambridge Univ. Press, Cambridge, U. K., and New York, doi:10.1017/CBO9781107415324.026.

Cornford, S. L., D. F. Martin, D. T. Graves, D. F. Ranken, A. M. Le Brocq, R. M. Gladstone, A. J. Payne, E. G. Ng, and W. H. Lipscomb (2013), Adaptive mesh, finite volume modeling of marine ice sheets, *J. Comput. Phys.*, *232*(1), 529–549, doi:10.1016/j.jcp.2012.08.037.

Fowler, A. C. (2010), Weertman, Lliboutry and the development of sliding theory, *J. Glaciol.*, *56*(200), 965–972.

Fretwell, P., et al. (2013), Bedmap2: Improved ice bed, surface and thickness datasets for Antarctica, *Cryosphere*, *7*(1), 375–393, doi:10.5194/tc-7-375-2013.

Gillet-Chaulet, F., O. Gagliardini, H. Seddik, M. Nodet, G. Durand, C. Ritz, T. Zwinger, R. Greve, and D. G. Vaughan (2012), Greenland ice sheet contribution to sea-level rise from a new-generation ice-sheet model, *Cryosphere*, *6*(6), 1561–1576, doi:10.5194/tc-6-1561-2012.

Goldberg, D. N. (2011), A variationally derived, depth-integrated approximation to a higher-order glaciological flow model, *J. Glaciol*, *57*(201), 157–170.

Goldberg, D. N., and P. Heimbach (2013), Parameter and state estimation with a time-dependent adjoint marine ice sheet model, *Cryosphere Discuss.*, *7*, 2845–2890, doi:10.5194/tcd-7-2845-2013.

Heimbach, P., and V. Bugnion (2009), Greenland ice-sheet volume sensitivity to basal, surface and initial conditions derived from an adjoint model, *Ann. Glaciol.*, *50*(52), 67–80.

Hindmarsh, R. C. A. (2004), A numerical comparison of approximations to the Stokes equations used in ice sheet and glacier modeling, *J. Geophys. Res.*, *109*, F01012, doi:10.1029/2003JF000065.

Jay-Allemand, M., F. Gillet-Chaulet, O. Gagliardini, and M. Nodet (2011), Investigating changes in basal conditions of Variegated Glacier prior to and during its 1982–1983 surge, *Cryosphere*, *5*(3), 659–672, doi:10.5194/tc-5-659-2011.

Joughin, I., D. MacAyeal, and S. Tulaczyk (2004), Basal shear stress of the Ross ice streams from control method inversions, *J. Geophys. Res.*, *109*, B09405, doi:10.1029/2003JB002960.

Joughin, I., B. E. Smith, and B. Medley (2014), Marine ice sheet collapse potentially underway for the Thwaites glacier basin, West Antarctica, *Science*, *344*, 735–738, doi:10.1126/science.1249055.

Khazendar, A., E. Rignot, and E. Larour (2007), Larsen B Ice Shelf rheology preceding its disintegration inferred by a control method, *Geophys. Res. Lett.*, *34*, L19503, doi:10.1029/2007GL030980.

Kohn, R., and M. Vogelius (1984), Determining conductivity by boundary measurements, *Commun. Pure Appl. Math.*, *37*(3), 289–298.

Larour, E., J. Utke, B. Csatho, A. Schenk, H. Seroussi, M. Morlighem, E. Rignot, N. Schlegel, and A. Khazendar (2014), Inferred basal friction and surface mass balance of the Northeast Greenland Ice Stream using data assimilation of ICESat (Ice Cloud and land Elevation Satellite) surface altimetry and ISSM (Ice Sheet System Model), *Cryosphere*, *8*, 2335–2351, doi:10.5194/tc-8-2335-2014.

Larour, E., E. Rignot, I. Joughin, and D. Aubry (2005), Rheology of the Ronne Ice Shelf, Antarctica, inferred from satellite radar interferometry data using an inverse control method, *Geophys. Res. Lett.*, *32*, L05503, doi:10.1029/2004GL021693.

Le Brocq, A. M., A. J. Payne, and A. Vieli (2010), An improved Antarctic dataset for high resolution numerical ice sheet models (ALBMAP v1), *Earth Syst. Sci. Data*, *2*, 247–260.

Lliboutry, L. (1968), General theory of subglacial cavitation and sliding of temperate glaciers, *J. Glaciol.*, *7*, 21–58.

MacAyeal, D. R. (1989), Large-scale ice flow over a viscous basal sediment—Theory and application to Ice Stream-B, Antarctica, *J. Geophys. Res.*, *94*(B4), 4071–4087.

MacAyeal, D. R. (1992), The basal stress-distribution of Ice Stream-E, Antarctica, inferred by control methods, *J. Geophys. Res.*, *97*(B1), 595–603.

Maxwell, D., M. Truffer, S. Avdonin, and M. Stuefer (2008), An iterative scheme for determining glacier velocities and stresses, *J. Glaciol.*, *54*(188), 888–898.

McMillan, M., A. Shepherd, A. Sundal, K. Briggs, A. Muir, A. Ridout, A. Hogg, and D. Wingham (2014), Increased ice losses from Antarctica detected by CryoSat-2, *Geophys. Res. Lett.*, *41*, 3899–3905, doi:10.1002/2014GL060111.

Morland, L., and I. Johnson (1980), Steady motion of ice sheets, *J. Glaciol.*, *25*(92), 229–246.

Morlighem, M., E. Rignot, H. Seroussi, E. Larour, H. Ben Dhia, and D. Aubry (2010), Spatial patterns of basal drag inferred using control methods from a full-Stokes and simpler models for Pine Island Glacier, West Antarctica, *Geophys. Res. Lett.*, *37*, L14502, doi:10.1029/2010GL043853.

Morlighem, M., H. Seroussi, E. Larour, and E. Rignot (2013), Inversion of basal friction in Antarctica using exact and incomplete adjoints of a higher-order model, *J. Geophys. Res. Earth Surf.*, *118*, 1746–753, doi:10.1002/jgrf.20125.

Muszynski, I., and G. Birchfield (1987), A coupled marine ice-stream ice-shelf model, *J. Glaciol.*, *33*(113), 3–15.

Navier, C. (1823), Memoire sur les lois du mouvement des fluides, *Mem. Acad. R. Sci. Inst. France*, *6*, 389–440.

Paterson, W. (1994), *Physics of Glaciers*, 3rd ed., Pergamon, Oxford, U. K.

Pattyn, F. (2002), Transient glacier response with a higher-order numerical ice-flow model, *J. Glaciol.*, *48*(162), 467–477, doi:10.3189/172756502781831278.

Pattyn, F. (2010), Antarctic subglacial conditions inferred from a hybrid ice sheet/ice stream model, *Earth Planet. Sci. Lett.*, *295*(3–4), 451–461, doi:10.1016/j.epsl.2010.04.025.

Perego, M., M. Gunzburger, and J. Burkardt (2012), Parallel finite-element implementation for higher-order ice-sheet models, *J. Glaciol.*, *58*(207), 76–88, doi:10.3189/2012JoG11J063.

Petra, N., H. Zhu, G. Stadler, T. J. R. Hughes, and O. Ghattas (2012), An inexact Gauss-Newton method for inversion of basal sliding and rheology parameters in a nonlinear Stokes ice sheet model, *J. Glaciol.*, *58*(211), 889–903, doi:10.3189/2012JoG11J182.

Pettit, E. C., E. D. Waddington, W. D. Harrison, T. Thorsteinsson, D. Elsberg, J. Morack, and M. A. Zumberge (2011), The crossover stress, anisotropy and the ice flow law at Siple Dome, West Antarctica, *J. Glaciol.*, *57*(201), 39–52.

Pollard, D., and R. M. DeConto (2012), A simple inverse method for the distribution of basal sliding coefficients under ice sheets, applied to Antarctica, *Cryosphere*, *6*(5), 953–971, doi:10.5194/tc-6-953-2012.

Pritchard, H. D., R. J. Arthern, D. G. Vaughan, and L. A. Edwards (2009), Extensive dynamic thinning on the margins of the Greenland and Antarctic ice sheets, *Nature*, *461*(7266), 971–975, doi:10.1038/nature08471.

Raymond, M. J., and G. H. Gudmundsson (2009), Estimating basal properties of ice streams from surface measurements: A non-linear Bayesian inverse approach applied to synthetic data, *Cryosphere*, *3*(2), 265–278, doi:10.5194/tc-3-265-2009.

Rignot, E., J. Mouginot, and B. Scheuchl (2011), Ice flow of the Antarctic ice sheet, *Science*, *333*(6048), 1427–1430, doi:10.1126/science.1208336.

Rommelaere, V., and D. R. MacAyeal (1997), Large-scale rheology of the Ross Ice Shelf, Antarctica, computed by a control method, *Ann. Glaciol.*, *24*, 43–48.

Schafer, M., T. Zwinger, P. Christoffersen, F. Gillet-Chaulet, K. Laakso, R. Pettersson, V. A. Pohjola, T. Strozzi, and J. C. Moore (2012), Sensitivity of basal conditions in an inverse model: Vestfonna ice cap, Nordaustlandet/Svalbard, *Cryosphere*, *6*(4), 771–783, doi:10.5194/tc-6-771-2012.

Schoof, C. (2005), The effect of cavitation on glacier sliding, *Proc. R. Soc. London, Ser. A*, *461*(2055), 609–627, doi:10.1098/rspa.2004.1350.

Schoof, C. (2007), Marine ice-sheet dynamics. Part 1: The case of rapid sliding, *J. Fluid Mech.*, *573*, 27–55, doi:10.1017/S0022112006003570.

Schoof, C. (2010), Coulomb friction and other sliding laws in a higher-order glacier flow model, *Math. Models Methods Appl. Sci.*, *20*(1), 157–189, doi:10.1142/S0218202510004180.

Schoof, C., and R. C. A. Hindmarsh (2010), Thin-film flows with wall slip: An asymptotic analysis of higher order glacier flow models, *Q. J. Mech. Appl. Math.*, *63*(1), 73–114, doi:10.1093/qjmam/hbp025.

Sergienko, O. V., T. T. Creyts, and R. C. A. Hindmarsh (2014), Similarity of organized patterns in driving and basal stresses of Antarctic and Greenland ice sheets beneath extensive areas of basal sliding, *Geophys. Res. Lett.*, *41*, 3925–3932, doi:10.1002/2014GL059976.

Sweldens, W. (1998), The lifting scheme: A construction of second generation wavelets, *SIAM J. Math. Anal.*, *29*(2), 511–546, doi:10.1137/S0036141095289051.

Tarasov, L., A. S. Dyke, R. M. Neal, and W. R. Peltier (2012), A data-calibrated distribution of deglacial chronologies for the North American ice complex from glaciological modeling, *Earth Planet. Sci. Lett.*, *315*, 30–40, doi:10.1016/j.epsl.2011.09.010.

van Pelt, W. J. J., J. Oerlemans, C. H. Reijmer, R. Pettersson, V. A. Pohjola, E. Isaksson, and D. Divine (2013), An iterative inverse method to estimate basal topography and initialize ice flow models, *Cryosphere*, *7*(3), 987–1006, doi:10.5194/tc-7-987-2013.

Vasilyev, O., and N. Kevlahan (2005), An adaptive multilevel wavelet collocation method for elliptic problems, *J. Comput. Phys.*, *206*(2), 412–431, doi:10.1016/j.jcp.2004.12.013.

Vaughan, D., et al. (2013), Observations: Cryosphere, in *Climate Change 2013: The Physical Science Basis. Contribution of Working Group I to the Fifth Assessment Report of the Intergovernmental Panel on Climate Change*, edited by T. F. Stocker et al., chap. 4, pp. 317–382, Cambridge Univ. Press, Cambridge, U. K., and New York, doi:10.1017/CBO9781107415324.012.

Vieli, A., and A. J. Payne (2003), Application of control methods for modelling the flow of Pine Island Glacier, West Antarctica, *Ann. Glaciol.*, *36*, 197–204, doi:10.3189/172756403781816338.

Vieli, A., A. J. Payne, A. Shepherd, and Z. Du (2007), Causes of pre-collapse changes of the Larsen B ice shelf: Numerical modelling and assimilation of satellite observations, *Earth Planet. Sci. Lett.*, *259*(3–4), 297–306, doi:10.1016/j.epsl.2007.04.050.

Vogel, S., S. Tulaczyk, B. Kamb, H. Engelhardt, F. Carsey, A. Behar, A. Lane, and I. Joughin (2005), Subglacial conditions during and after stoppage of an Antarctic Ice Stream: Is reactivation imminent?, *Geophys. Res. Lett.*, *32*, L14502, doi:10.1029/2005GL022563.

Weertman, J. (1964), The theory of glacial sliding, *J. Glaciol*, *5*, 287–303.

Williams, C. R., R. C. A. Hindmarsh, and R. J. Arthern (2012), Frequency response of ice streams, *Proc. R. Soc. London, Ser. A*, *468*(2147), 3285–3310, doi:10.1098/rspa.2012.0180.

Williams, C. R., R. C. A. Hindmarsh, and R. J. Arthern (2014), Calculating balance velocities with a membrane stress correction, *J. Glaciol.*, *60*(220), 294–304.

Wingham, D. J., A. Shepherd, A. Muir, and G. J. Marshall (2006), Mass balance of the Antarctic ice sheet, *Philos. Trans. R. Soc. A*, *364*(1844), 1627–1635, doi:10.1098/rsta.2006.1792.

Wright, A., and M. Siegert (2012), A fourth inventory of Antarctic subglacial lakes, *Antarct. Sci.*, *24*(6), 659–664, doi:10.1017/S095410201200048X.